PERGAMON

Electrochimica Acta 45 (1999) 295–314

ELECTROCHIMICA Acta

www.elsevier.nl/locate/electacta

Synthesis, characterization and cell performance of inverse spinel electrode materials for lithium secondary batteries

George Ting-Kuo Fey*, Donp-Liang Huang

Department of Chemical Engineering, National Central University, Chung-Li, Taiwan ROC

Received 14 February 1999; received in revised form 11 May 1999

Abstract

The preparation methods, materials' characterization, and electrochemical properties of inverse spinel materials, such as $LiNiVO_4$, $LiCoVO_4$, and $LiNi_yCo_{1-y}VO_4$, are reviewed. The preparation methods include conventional ceramic sintering, solution co-precipitation, sol-gel, and hydrothermal methods. Recent structural results for these materials obtained from XRD, IR, Raman, ^{7}Li NMR, EXAFS, and XANES analyses are presented. Their electrochemical properties in terms of cyclic voltammetry, electrical conductivity, cathode and anode performance were also discussed.

Keywords: $LiNiVO_4$; $LiCoVO_4$; High-voltage cathode materials; Inverse spinel; Anode materials; Lithium secondary batteries; XRD; FTIR; Cyclic voltammetry

1. Introduction

Since the early 1960s, research on $LiMVO_4$ materials has focused on its preparation and characterization, where M = Cu, Ni, Co, Zn, Cd, Mg, and Be [1–5]. Based on early results [4,6,7], the $LiMVO_4$ compounds were shown to have three different structures: (1) spinel, (2) olivine, or (3) phenacite. Both $LiNiVO_4$ and $LiCoVO_4$ were considered for decades to be spinel, but our calculations, using recent powder XRD results, have explicitly shown that they are actually inverse spinel [8]. Recently, we have learned of earlier reports concerning lithium insertion into $LiFe_5O_8$ and Fe_3O_4 [9,10], whose description also fitted an inverse spinel structure. Interestingly, $LiNiVO_4$ not only exhibits a voltage of 4.8 V, the first known Li intercalation reaction observed near 5 V, but it is also the first material with an inverse spinel structure to be patented as a potential cathode material for rechargeable lithium cells [11]. Until now, little attention has been directed toward battery applications because of insufficient structural understanding and high-voltage resistant electrolyte availability.

The so-called 'rocking chair' batteries [12], whose anodes employ non-lithium metal materials, such as carbon [13], lithium metal oxide [14] or a lithium alloy [15,16], which can intercalate lithium ion reversibly, have been proposed to contain the problems with lithium metal dendritic growth and to improve the safety of rechargeable lithium batteries. As a result of replacing the lightweight metallic lithium anode, the rocking-chair battery system must then use high-voltage cathode materials (ca 4 V vs Li metal) in order to increase its energy density and compensate for the increase in anode weight and potential. $LiCoO_2$, $LiNiO_2$ and $LiMn_2O_4$ compounds have been developed and marketed for lithium 'rocking-chair' batteries [17–

* Corresponding author. Tel.: +886-3-422-7151; fax: +886-3-425-7325.

E-mail address: gfey@cc.ncu.edu.tw (G. Ting-Kuo Fey)

0013-4686/99/$ - see front matter
PII: S0013-4686(99)00212-1

Table 1
Preparation methods and reaction conditions for $LiMVO_4$ compounds

Compound	Scheme	Reactants	Reaction conditions	Ref.	Year
$LiNiVO_4$	1[b]	$LiVO_3 + NiCO_3$	500°C, 7 days	[1]	1961
	2[b]	$LiVO_3 + NiO$	1000°C, 100 h	[34]	1979
	3[b]	$Li_2O + 2NiO + V_2O_5$	800°C, 1 day to 550°C, 25 days	[28]	1988
	4[b]	$Li_2CO_3 + 2NiCO_3 + V_2O_5$	700°C, 12 h	[35]	1994
	5[b]	$Li_2CO_3 + 2NiO + V_2O_5$	650°C, 18 h	[35]	1994
	6[a]	$2LiOH{\cdot}H_2O + 2Ni(NO_3)_2{\cdot}6H_2O + V_2O_5$	700°C, 6 h	[35]	1994
	7[a]	$LiOH{\cdot}H_2O + Ni(NO_3)_2{\cdot}6H_2O + NH_4VO_3$	800°C, 12 h	[35]	1994
	8[b]	$2LiNiO_2 + V_2O_5$	700°C, 2 h	[8]	1994
	9[b]	$Li_2CO_3 + 2NiO + V_2O_5$	730°C, 12 h	[36]	1995
	10[a]	$LiOH{\cdot}H_2O + Ni(NO_3)_2{\cdot}6H_2O + NH_4VO_3$	400°C, 192 h or 500°C, 48 h	[36]	1995
	11[b]	$2LiNiO_2 + V_2O_3$	500°C, 4 h and 800°C, 6 h	[26]	1997
	12[b]	$LiNO_3 + Ni(NO_3)_2{\cdot}6H_2O + NH_4VO_3 + 6NH_2CH_2COOH$	350°C and 500°C, 6 h	[22]	1997
	13[a]	$7LiNO_3$ (in excess) $+ 0.45Ni(NO_3)_2{\cdot}6H_2O + 0.25\ NH_4VO_3$	200–700°C, 12 h	[23]	1998
	14[a]	$LiNO_3 + Ni(NO_3)_2{\cdot}6H_2O + V(C_5H_7O_2)_3$	450°C, 12 h	[29]	1998
	15[a]	$LiOH{\cdot}H_2O + Ni(CH_3COO)_2{\cdot}4H_2O + NH_4VO_3$	200°C, ca 15 atm for 2 h	[30]	1998
$LiCoVO_4$	16[b]	$LiVO_3 + CoC_2O_4$	500°C, 7 days	[1]	1961
	17[b]	$3Li_2CO_3 + 2Co_3O_4 + 3\ V_2O_5$	650°C, 18 h	[35]	1994
	18[b]	$2LiCoO_2 + V_2O_3$	700°C, 2 h	[8]	1994
	19[a]	$LiOH{\cdot}H_2O + Co(NO_3)_2{\cdot}6H_2O + NH_4VO_3$	400°C, 192 h or 500°C, 48 h	[36]	1995
	20[b]	$2LiCoO_2 + V_2O_3$ or V_2O_5	700°C, 1 h	[26]	1997
$LiMgVO_4$		$Li_2CO_3 + 2MgCO_3 + 2NH_4VO_3$	750°C, 1 day	[4]	1964
		$Li_2CO_3 + 2MgO + 2NH_4VO_3$	650°C, 4 days	[6]	1974
		$Li_2O + 2MgO + V_2O_5$	800°C, 1 day to 500°C, 25 days	[28]	1988
$LiZnVO_4$		$Li_2CO_3 + 2ZnO + 2NH_4VO_3$	750°C, 1 day	[4]	1964
		$Li_2CO_3 + 2ZnO + V_2O_5$	500–700°C	[31]	1980
		$Li_2O + 2ZnO + V_2O_5$	800°C, 1 day to 500°C, 25 days	[28]	1988
$LiBeVO_4$		$Li_2CO_3 + 2BeO + 2NH_4VO_3$	750°C, 1 day	[4]	1964
$LiCdVO_4$		$Li_2CO_3 + 2CdCO_3 + 2NH_4VO_3$	600°C, 8 days	[6]	1974
$LiCuVO_4$		$Li_2CO_3 + 2CuO + V_2O_5$	530°C, 7 days	[32]	1991
$LiMnVO_4$		$Li_2CO_3 + Mn_2O_3 + 2NH_4VO_3$	650°C, 100 h	[33]	1997

[a] Solution–coprecipitation method.
[b] High-temperature solid-state process.

20]. Both the $LiCoO_2$ and $LiNiO_2$ compounds have a layered structure while $LiMn_2O_4$ has a spinel structure.

However, high-voltage cathode materials are strong oxidizers, which may create electrolyte degradation problems. In order to overcome such problems and to understand the effects of replacing nickel by cobalt in $LiNiVO_4$, we prepared and characterized a series of $LiNi_yCo_{1-y}VO_4$ (y = 0.1–0.9) compounds. Structural analysis has revealed these compounds to be inverse spinel, with the cubic lattice constant, a, varying as a linear function with the stoichiometry, y, in $LiNi_yCo_{1-y}VO_4$ [21].

Since the discovery of these new inverse spinel cathode materials for rechargeable lithium batteries, interest in them has increased due to their high voltage behavior. Prabaharan et al. [22] described a simple procedure called the aqueous glycine-nitrate precursor method for preparing single-phase $LiNiVO_4$, at temperatures as low as 320°C, for use as a cathode-active material in secondary lithium batteries, but cell capacity was not discussed. Orsini et al. [23] prepared amorphous and crystallized $LiNiVO_4$ at low temperatures and reported their electrochemical properties vs. Li when used as negative electrodes in lithium-ion batteries. The $LiNiVO_4$ anode displays reversible capacities as large as 900 mAh/g when prepared by a new 'chimie douce' method, consisting of a precipitation reaction at pH = 8.5 and annealing at different temperatures from 85 to 700°C. Both amorphous and crystallized $LiNiVO_4$ can react reversibly with a 7 Li per formula unit, similar to compounds synthesized by the traditional high-temperature route [23].

Introducing rare earth atoms into the $LiNiVO_4$ inverse spinel structure can improve the electrical conductivity. For instance, Yb-doped samples at 25°C showed the greatest improvement in conductivity, by a factor of three, an increase from 10^{-10} to 10^{-7} S/cm [24]. Dopant effects were studied by measuring the

electrical conductivity of $LiNiVO_4$ as a function of temperature, type of dopants, and dopant ratio. The dopant mole ratios of $LiNiVO_4$ to Ln (where Ln = La, Gd, or Yb), used in the reactions of $LiOH{\cdot}H_2O$, NH_4VO_3, $Co(NO_3)_2{\cdot}6H_2O$ and Ln_2O_3, ranged from 1×10^6 to 1×10^2 [24].

Padhi et al. [25] have reported that $LiMnVO_4$ exists in two forms: ambient-pressure $LiV[Mn]O_4$ and high-pressure cubic-spinel phase $V[LiMn]O_4$. The former is an orthorhombic phase, which had two of the three cations on tetrahedral sites and was transformed under pressure into a cubic spinel structure $V[LiMn]O_4$ in which the $(VO_4)^{3-}$ ions act as polyanions. The so-called high-pressure cubic-spinel phase $V[LiMn]O_4$ is consistent with an inverse spinel structure in which Li and Mn atoms are located among octahedral sites. The redox energy of the Mn^{3+}/Mn^{2+} couple lies 3.8 eV below the Fermi energy of elemental lithium, more stable than the Mn^{4+}/Mn^{3+} redox energy at 3.0 eV in $Li[Mn_2]O_4$.

The goal of this paper is to review recent work on the properties of $LiNiVO_4$ materials and its related compounds such as $LiCoVO_4$ and $LiNi_yCo_{1-y}VO_4$, including preparation methods, material characteristics, and applications as electrode materials. In the last couple of years, research conducted on the fundamental structure and electrochemical properties of these cathode and anode materials has produced some good results. Further details of these recent developments that are not covered in this review can be found in references [8,21–25].

2. Synthesis and reactions

Table 1 presents some typical examples of preparation methods for $LiMVO_4$ materials, where M = Ni [1,8,22,23,26,28–30,34–36], Co [1,8,26,35,36], Zn [3,4,28,31], Mg [4,6,28], Be [4], Cd [6], Mn [25,33], Cu [27,32], etc., including reactants, reaction conditions, references, and publication year. Most materials are generally prepared by high-temperature solid-state reaction methods or classical ceramic methods of powder mixing, pressing and heating. The preparation methods marked with a superscript a in Table 1 utilized a low-temperature solution–coprecipitation process, whereas the methods with superscript b employed a high-temperature solid-state process. Most of the synthesis methods with superscript a in the scheme numbers will be discussed in greater detail in this Section, because their products are potential cathode and anode materials for lithium secondary batteries.

Schemes 1 and 2, used almost four decades ago, were not economically practical because of the long reaction time and high temperature required. To develop a new and more practical method, we have proposed a novel way of preparing $LiNiVO_4$ [8,26] through a solid state reaction of $LiNiO_2$ and V_2O_3 or V_2O_5 (schemes 8 and 11). In order to determine the optimum reaction conditions, a series of solid-state reactions with different starting materials, reaction atmospheres, reactant stoichiometries, and synthesis temperatures was carried out. $LiNiO_2$ and V_2O_5 reacting in air at 700°C for 2 h was found to be the best method. Details of these results were reported in [26]. Similarly, the isostructural compound $LiCoVO_4$ can be synthesized using scheme 20. Since both $LiNiVO_4$ and $LiCoVO_4$ can be prepared in no more than 2 h, this new method has the potential to be a practical process for producing a large quantity of good quality $LiMVO_4$ (M = Ni or Co).

The effects of the stoichiometry and synthesis temperature on the reactions of $Li_xNi_{2-x}O_2$ ($0.25 < x < 1.03$) and V_2O_3 in air were investigated [37]. Based on the XRD results of the above reactions, single-phase samples were obtained for $x = 0.75$–1.00 and there is no evidence that nonstoichiometric $Li_xNi_{2-x}VO_4$ was ever formed [37]. When lithium or nickel was stoichiometrically deficient with $x < 0.75$, a complicated mixture of Li_3VO_4, NiV_2O_7, and $Ni_3(VO_4)_2$ was formed in addition to $LiNiVO_4$. On the other hand, when lithium or nickel was stoichiometrically excessive, impurities such as Li_3VO_4 and NiO were formed. By comparing synthesis temperatures ranging from 600 to 975°C, we determined that 800°C was the optimal preparation temperature for pure $LiNiVO_4$, because $LiVO_3$ impurities were formed between 600 and 700°C and NiO impurities were formed at >900°C.

The main disadvantages of the solid-state method are that solid particles may not react completely, producing impurities, and that sintering temperatures must be high. However, these problems can be overcome by using low-temperature solution-coprecipitation or sol-gel methods.

The synthesis of $LiNiVO_4$, using the aqueous glycine-nitrate combustion process, where glycine-nitrate acts as a fuel for spontaneous decomposition, has also been investigated [22]. The ratio of glycine to starting materials such as $LiNO_3$, $Ni(NO_3)_2$, and NH_4VO_3 in the mixture was 2:1 (scheme 12). This aqueous glycine-nitrate precursor method provides a simple procedure for preparing bulk quantities of submicron-sized particles of electrochemically active single-phase $LiNiVO_4$ at a low temperature of 320°C.

A 'chimie douce' method [38], previously developed for the synthesis of amorphous RVO_4 (R = In, Fe, Cr, Al, etc.), was employed to synthesize yellowish-green amorphous $LiNiVO_4$ by conducting a precipitation reaction at pH = 8.5 in a solution where the mole ratio of Li to Ni was in excess by a factor of 15 (scheme 13) [23]. Furthermore, the amorphous precursor could be

Table 2
Types of structures of $LiMVO_4$ compounds [4,6,26,33]

Structure	Compounds
Spinel	$LiCuVO_4$, $LiMnVO_4$, $LiNiVO_4$[a], $LiCoVO_4$[a]
Olivine	$LiMnVO_4$, $LiCdVO_4$, $LiMgVO_4$
Phenacite	$LiBeVO_4$, $LiZnVO_4$

[a] Both $LiNiVO_4$ and $LiCoVO_4$ are shown to be inverse spinel from our recent results [8].

progressively crystallized by increasing the annealing temperature from 200 to 700°C. Both the amorphous and crystallized $LiNiVO_4$ showed electrochemical behavior, similar to the compounds prepared by the classical ceramic route.

The morphology of ultrafine $LiNiVO_4$ powders prepared by a low-temperature solution-coprecipitation process (scheme 14) was analyzed in our new work [29]. A comparison of the morphology and the grain size of products prepared under acidic (pH: 3), neutral (pH: 7) and basic (pH: 11) conditions was performed. The overall grain size was quite small, ranging from 0.1 to 1 μm. A series of $LiNiVO_4$ products having various pH values, ranging from 1 to 6, was prepared to study the effects of the pH value on the properties of $LiNiVO_4$ and its cell performance as a cathode material. From XRD analysis, $LiNiVO_4$, was found to have a single phase for pH = 1–5, but contained NiO impurities for pH = 6. The SEM results showed that the product had small particles with a narrow distribution range, but the particle size increased as the pH value increased. BET measurements showed that the surface area of the powder products decreased as their pH values increased.

In order to reduce the reaction temperature and preparation time for $LiNiVO_4$ powder, a newly developed hydrothermal method, scheme 15, was used [30]. The particle size of the resultant powders ranged from 0.2 to 0.3 μm.

Apart from the $LiNiVO_4$ and $LiCoVO_4$ compounds described in Table 1, a series of $LiNi_yCo_{1-y}VO_4$ (y = 0.1–0.9) compounds were synthesized by a high-temperature solid-state reaction (the HT-method) of $LiNi_yCo_{1-y}O_2$ and V_2O_5 at 800°C for 12 h, or a low-temperature solution-coprecipitation reaction (the LT-method) of $LiOH{\cdot}H_2O$, $Ni(NO_3)_2{\cdot}6H_2O$, $Co(NO_3)_2{\cdot}6H_2O$ and NH_4VO_3, heating the precipitates at 500°C for 48 h [21]. The products from both preparation methods were then characterized by XRD, SEM, and ICP-AES. From the SEM results, the grain-size distribution of LT-$LiNi_yCo_{1-y}VO_4$ was in the 0.1–1 μm range, whereas that of HT-$LiNi_yCo_{1-y}VO_4$ was in the 5–30 μm range. From the ICP-AES analysis, the lithium stoichiometry in both the LT- and the HT-$LiNi_yCo_{1-y}VO_4$ samples was slightly deficient, ranging from 0.932 to 0.950 and from 0.910 to 0.925 for the LT- and HT-samples, respectively. The errors in these ICP-AES results were about 3%.

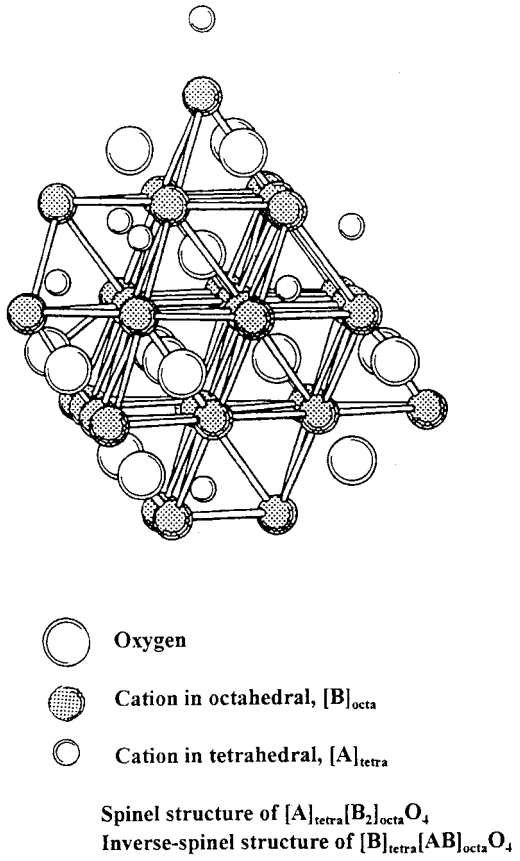

Fig. 1. Spinel and inverse-spinel structures of AB_2O_4 compounds.

3. Structure and characterization

3.1. Structural and XRD analysis

Table 2 shows the type of structure possessed by $LiMVO_4$ compounds. Interestingly, the olivine structure of both $LiMgVO_4$ and $LiZnVO_4$ at atmospheric pressure can be transformed to a cubic spinel structure under pressure [3,4]. Similarly, $LiMnVO_4$ also possesses two structures: an orthorhombic $LiV[Mn]O_4$ phase under ambient pressure and a cubic-spinel $V[LiMn]O_4$ phase under high-pressure (P = 55 kbar) [25]. However, powder XRD data calculations in our recent studies have shown that both $LiNiVO_4$ and $LiCoVO_4$ are inverse spinels.

Fig. 1 shows the atom arrangement and site lo-

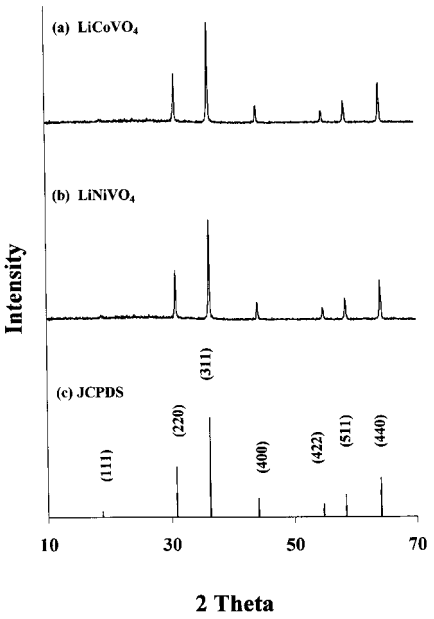

Fig. 2. The XRD patterns of $LiNiVO_4$ and $LiCoVO_4$ prepared by a solution–coprecipitation method [36].

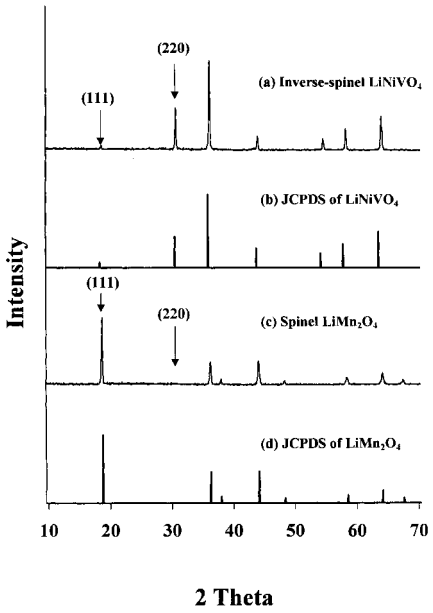

Fig. 3. The XRD patterns of a normal spinel and an inverse spinel.

cations for AB_2O_4 oxides with either spinel or inverse spinel structures. In a normal spinel such as $LiMn_2O_4$, the oxygen atoms are in a closely packed cubic array with the transition metal atoms residing at the interstices, forming an octahedron with the six closest oxygen atoms. The lithium atoms also reside at the interstices, forming a tetrahedron with the four neighboring oxygen atoms. In reality, this description is a simplification and the two cation distributions quoted are only an ideal. Usually, some cation mixing of metals on various sites is quite common.

Spinel materials such as $LiTi_2O_4$ and $LiMn_2O_4$ [39,40] are known to reversibly intercalate lithium. In an inverse spinel, such as $LiNiVO_4$, the cations are arranged as $V_{tetra}(LiNi)_{octa}O_4$. The Li and Ni atoms are believed to be distributed equally and randomly in the octahedrally coordinated interstices and the V atoms are believed to occupy the tetrahedrally coordinated interstices. Based on previous work, the oxidation states of the cations are believed to be Li^{1+}, Ni^{2+}, and V^{5+} [41]. Unlike $LiMn_2O_4$, the intercalation occurring within $LiNiVO_4$ is unexpected because there are no obvious tunnels through which the mobile Li atoms can move.

Fig. 2 displays the XRD patterns and JCPDS files for $LiNiVO_4$ and $LiCoVO_4$. Both compounds were prepared by a reaction of $LiOH.H_2O$, $M(NO_3)_2{\cdot}6H_2O$ (where M = Ni or Co) and NH_4VO_3 via a solution–coprecipitation method at 500°C for 48 h. A simple comparison with the JCPDS' file confirms that the XRD patterns of both $LiNiVO_4$ and $LiCoVO_4$ are identical to each other and match the JCPDS' file, indicating that they are single phase and possess a similar structure.

Fig. 3 exhibits the major difference between the XRD patterns of a normal spinel and an inverse spinel. In normal spinels like $LiMn_2O_4$, the (111) peak intensity is the strongest peak in the pattern while the (220) peak is very weak. However, for inverse spinels such as $LiNiVO_4$, the (220) peak is much stronger than the (111) peak. The increase in the (220) peak intensity at the expense of the (111) peak can be explained by the presence of transition metal atoms on the tetrahedrally coordinated interstices.

Despite the quality of the pattern matching, the Rietveld analysis results are even more convincing in the structural determination process. Several XRD data for pure $LiNiVO_4$ were selected for Rietveld profile refinement analysis. In our earlier work, the data and calculations were a reasonable but not a perfect fit to an inverse spinel structure [8]. We later discovered that a thorough grinding would improve the sampling method for the Rietveld XRD-profile refinement analysis [37]. Because $LiNiVO_4$ is a highly crystalline material, the effect of crystal orientation on the XRD profiles is significant. Fig. 4 shows the effect of grinding on the XRD patterns of $LiNiVO_4$. Before grinding, Fig. 4(a), the Bragg peaks near 55, 58 and 64° appeared as doublets, which were very sensitive to changes in crystal orientation. Presumably, the split-

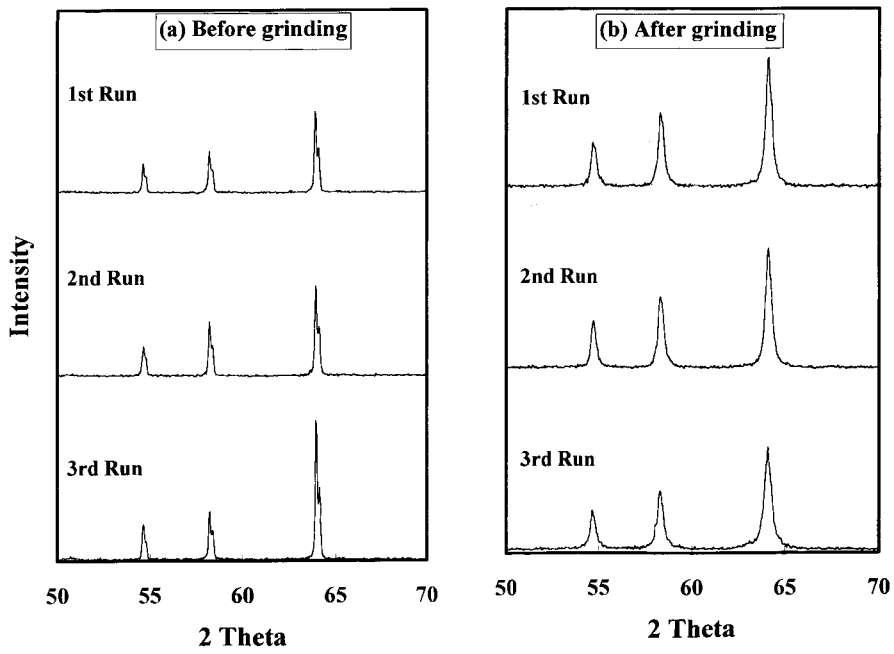

Fig. 4. The effect of grinding on the XRD patterns of $LiNiVO_4$: (a) before grinding; (b) after grinding [37].

tings in the peaks in Fig. 4(a) are due to $K_{\alpha 1}$ and $K_{\alpha 2}$ radiation. After grinding, these three peaks appeared as singlets with a constant relative intensity ratio, as shown in Fig. 4(b). After grinding, the largest difference between the measured and calculated pattern was less than 2%. The Bragg *R*-factor was 1.18, confirming that the structure of $LiNiVO_4$ was indeed inverse spinel. Fig. 5 illustrates the differences in the Rietveld profile refinement analysis for the powder XRD patterns of $LiNiVO_4$ before and after grinding.

In situ X-ray diffraction (XRD) data [8] showed that when Li is removed, the crystal lattice contracts and when Li is reinserted, it returns to its original structure. Fig. 6 demonstrates that $Li_{1-x}NiVO_4$ is not destroyed during charging beyond 4.8 V up to at least 5.3 V [8]. The voltage of the cell for each scan in Fig. 6 is indicated as D for discharge and C for charge. The scans have been offset vertically for clarity. Our findings prove that an intercalation reaction occurred in $Li/LiNiVO_4$ cells at a plateau near 4.8 V, but we still do not know why the voltage of the $Li/LiNiVO_4$ cell is so high. The iso-structural compound, $LiCoVO_4$, also de-intercalates Li, but at a much lower voltage, near 4.2 V [8]. Similar in situ XRD measurements for an electrochemical cell using $LiNiVO_4$ annealed at 600°C as the cathode and Li as the anode were reported, with an emphasis on the mechanism which occurred during cycling [23].

The XRD patterns for $LiNi_yCo_{1-y}VO_4$ (y = 0–1) prepared by the HT-method and the LT-method are displayed in Figs. 7 and 8, respectively [21]. For $0 < y < 1$, both the HT- and LT-$LiNi_yCo_{1-y}VO_4$ compounds are essentially single-phase and have inverse spinel-like XRD patterns identical to those of their parent compounds, $LiNiVO_4$ and $LiCoVO_4$. In order to confirm that the whole series of $LiNi_yCo_{1-y}VO_4$ ($0 < y < 1$) compounds is a solid solution of $LiNiVO_4$ and $LiCoVO_4$, the cubic lattice constant a was calculated for the whole series, based on the XRD data for the above mentioned spectra. Fig. 9 demonstrates that the cubic lattice constant a is a linear function of the stoichiometry y in $LiNi_yCo_{1-y}VO_4$ ($0 < y < 1$), confirming that the whole series is a solid solution of $LiNiVO_4$ and $LiCoVO_4$ with the corresponding stoichiometry [21].

3.2. Vibrational spectroscopy

The room-temperature Raman scattering and FTIR absorption spectra of single-phase $LiNiVO_4$ annealed at 500°C [22] are presented in Figs. 10 and 11, respectively. For a cubic spinel, the structure possesses prototypic Fd3 m (O_h^7) symmetry and yields nine vibrational modes, in which five modes symmetrical with the inversion center are Raman-active ($A_{1g}+E_g+3F_{2g}$) and four asymmetrical to the inversion center are IR-active ($4F_{1u}$).

As seen in Fig. 10, a strong broad band in the 700–850 cm^{-1} region is ascribable to the stretching frequencies of the VO_4 tetrahedron, a vibration between the

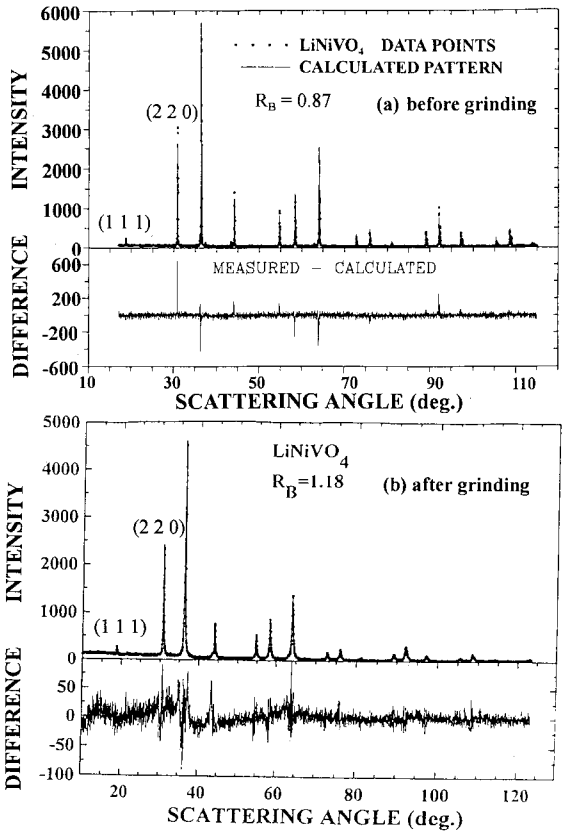

Fig. 5. Rietveld profile refinement analysis for the powder XRD patterns of $LiNiVO_4$: (a) before grinding; (b) after grinding [37].

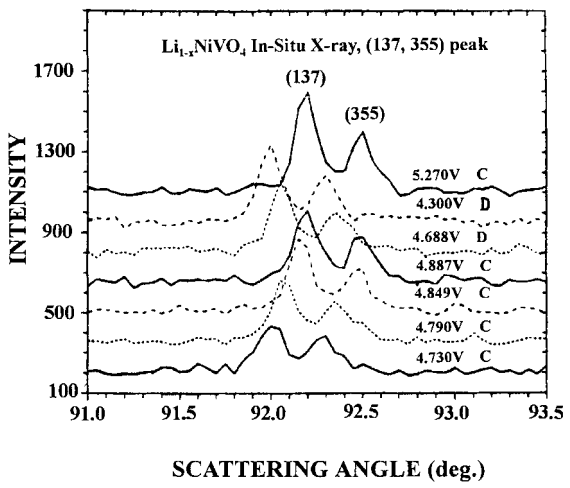

Fig. 6. The {137, 355} Bragg peak of $Li_{1-x}NiVO_4$ during cell cycling [8].

oxygen and the highest valency cation (V^{5+}). The high-frequency peak situated at 821 cm^{-1} is due to the stretching mode of the VO_4 tetrahedron with A_1 symmetry, while the band located at 335 cm^{-1} is attributable to the bending mode of the VO_4 tetrahedron with E symmetry. As expected, these vibrational modes are Raman-active. The broadness of the high-frequency band may be associated with the asymmetrical bonding of the VO_4 tetrahedron. Li and Ni may be bonded to each oxygen atom of a VO_4 tetrahedron, causing some asymmetry of the VO_4 unit but without affecting the molecular symmetry. In Fig. 11, two complex patterns of broad IR bands in the 300–500 and 600–1000 cm^{-1} regions are observed. These infrared-active bands are complementary to the Raman-active bands in Fig. 10. The vibrational assignments of the Raman and IR bands for inverse spinel $LiNiVO_4$ are presented in Table 3 [22].

A series of Raman spectra for $LiNi_yCo_{1-y}VO_4$ compounds (y = 0.1–0.9) were studied [42]. In order to determine a representative trend, $LiNi_{0.5}Co_{0.5}VO_4$ was selected since it is in the middle of the series. Fig. 12 shows the Raman spectra for $LiNi_{0.5}Co_{0.5}VO_4$ and their parent compounds, $LiNiVO_4$ and $LiCoVO_4$, to il-

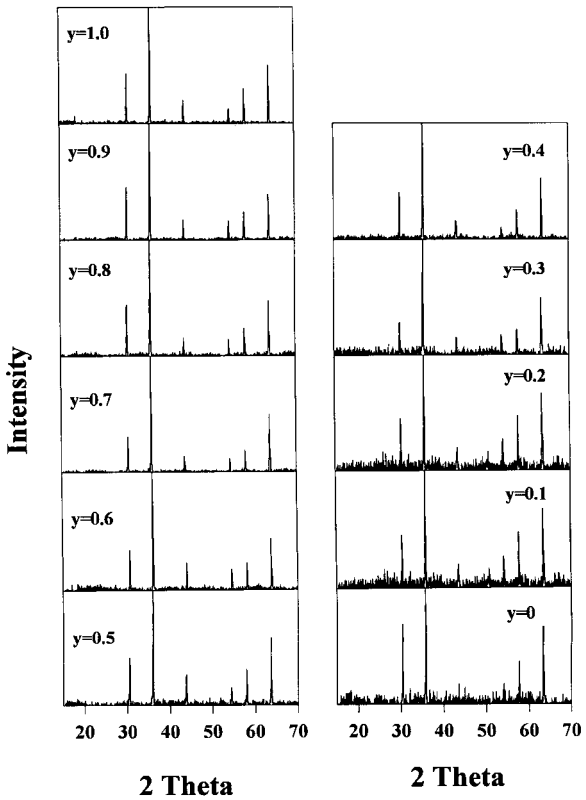

Fig. 7. The XRD patterns of $LiNi_yCo_{1-y}VO_4$ (y = 0–1) prepared by the HT-method [21].

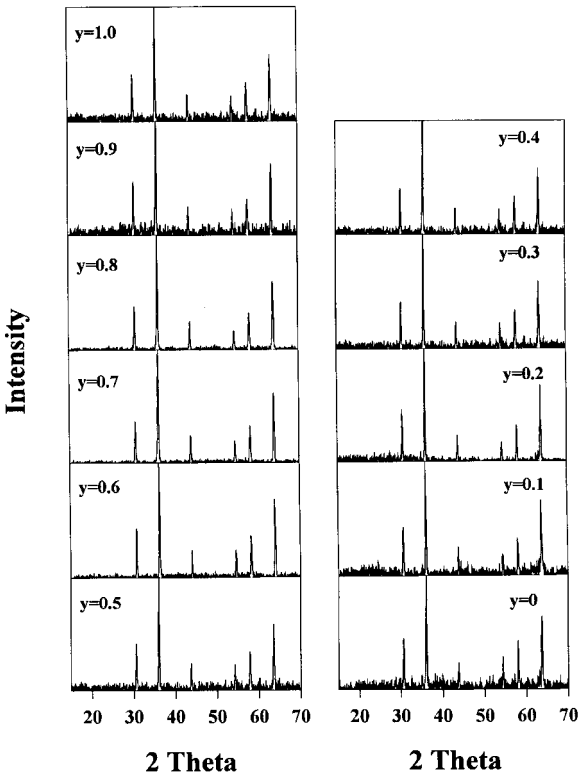

Fig. 8. The XRD patterns of $LiNi_yCo_{1-y}VO_4$ (y = 0–1) prepared by the LT-method [21].

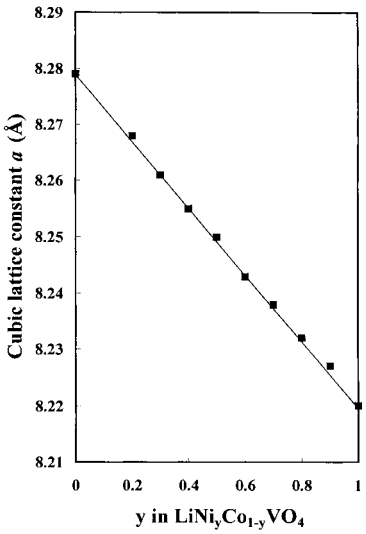

Fig. 9. The cubic lattice constant (L_a or a) as a function of stoichiometry (y) in $LiNi_yCo_{1-y}VO_4$ [21].

lustrate the effect of substituting Ni with Co in $LiNi_yCo_{1-y}VO_4$ on the vibrational modes of metal–oxygen bonding. A decrease in wavenumber for all vibrational modes of $LiNi_yCo_{1-y}VO_4$ was observed after the substitution of Ni by Co. This indicates that both V—O bonding in the VO_4 tetrahedron and M—O (where M = Li or Ni) bonding in the MO_6 octahedron are weakened as a result of substituting Co for Ni. A reduction in the bond strength between lithium and oxygen in an inverse spinel structure creates an easier environment for lithium movement, resulting in a lower voltage $LiCoVO_4$ material.

3.3. Solid-state ^{7}Li NMR spectroscopy

Solid-state ^{7}Li NMR spectroscopy is sensitive to local structural changes and suitable for monitoring Li environments with varying adjacent metal contents. The relevant structural characteristics, such as local bonding geometry, Li—O bond distance, O—Li—O dihedral angle, and local electric field gradient (efg), are readily reflected in the ^{7}Li static line shapes and the Magic Angle Spinning (MAS) side-band manifolds. ^{7}Li NMR is obtained from simple free decay after a single, strong radio-frequency pulse irradiation. The relaxation process is governed by the nuclear spin interactions (chemical shifts plus quadrupolar interactions) modulated by lithium motion. As the lithium motion is restricted within the framework, the Fourier transformation of the decay leads to the side-band manifolds revealing the size and the distribution of the lithium spins. Generally, line broadening in a static NMR spectrum is caused by chemical shift anisotropy (CSA), dipole–dipole interactions and quadrupolar interactions. Although solid-state ^{7}Li NMR spectroscopy

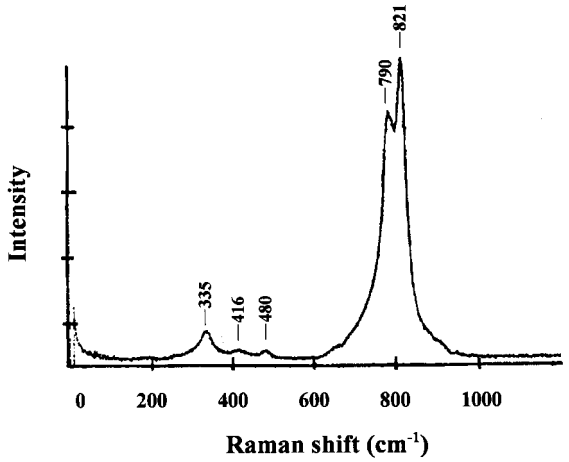

Fig. 10. Raman spectrum of inverse spinel $LiNiVO_4$ recorded at room temperature [22].

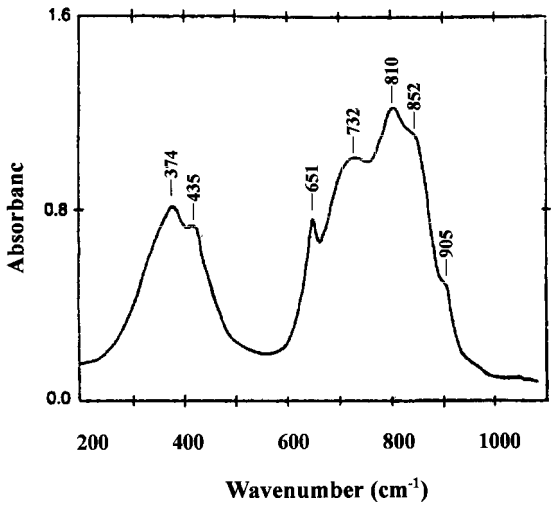

Fig. 11. FTIR spectrum of inverse spinel $LiNiVO_4$ recorded at room temperature [22].

is a useful technique for the micro-structural analysis of cathode materials in lithium ion batteries, only a few research papers covering this topic have been published [43–48].

Solid-state ^{7}Li NMR studies on the $LiNi_yCo_{1-y}VO_4$ microstructure to determine the coordination and distribution of Ni/Co cations and the surrounding Li were carried out by analyzing the MAS side-band manifolds [49]. The patterns of the central ^{7}Li transitions for $LiNi_yCo_{1-y}VO_4$ samples prepared by the HT and LT methods are shown in Figs. 13 and 14, respectively. Based on these NMR data, some parameters regarding the ^{7}Li NMR characteristics of $LiNi_yCo_{1-y}VO_4$ have been calculated. Table 4 summarizes the fitting results of isotropic chemical shift (δ_{ISO} or δ), chemical shift anisotropy (δ_{CSA}) and asymmetry parameter (η_{CSA} or η) with varying Ni/Co ratios, using a simple lattice model for both preparation methods. The asymmetry parameter is defined as a measure of the deviation of the chemical shift tensors from the axial symmetry; for example, in ^{7}Li NMR spectroscopy, $\eta = 0$ for an axially symmetric electron distribution around a lithium atom and $\eta = 1$ for a nonaxially symmetric electron distribution.

Table 4
The ^{7}Li NMR characteristics of $LiNi_yCo_{1-y}VO_4$ prepared by either the HT- or LT-method [49]

$LiNi_yCo_{1-y}VO_4$	HT method			LT method		
y	δ (ppm)	δ (kHz)	η_{CSA}	δ (ppm)	δ (kHz)	η_{CSA}
0.0	1.27	225	0.87	1.35	293	0.97
0.1	1.42	210	0.86	1.33	240	0.94
0.4	1.13	195	0.85	1.35	180	0.92
0.6	1.24	165	0.82	1.33	158	0.90
0.8	1.28	135	0.77	1.34	150	0.90
0.9	–	–	–	1.35	283	0.92
1.0	−2.13	300	0.60	–	–	–

As seen from Table 4, the isotropic chemical shift (δ) in LT-$LiNi_yCo_{1-y}VO_4$ compounds, from y = 0–0.9, remained almost constant at 1.33–1.35 ppm, whereas the δ in HT-$LiNi_yCo_{1-y}VO_4$ (y = 0–0.8) varied from 1.13 to 1.42 ppm. These results were consistent with randomly distributed Ni and Co in the octahedral cage of an inverse spinel for the less crystalline LT-samples. In addition, they also indicated that the Ni and Co distribution in highly crystalline HT-samples was not as random as in the LT-samples, but showed a more inhomogeneous distribution with an increasing Ni content.

As for the chemical shift anisotropy (δ_{CSA}) and the asymmetry parameter (η_{CSA}), both samples prepared by the HT or LT method showed a decreasing trend

Table 3
The vibrational assignments of Raman and IR bands of $LiNiVO_4$ [22]

Raman wavenumber (cm^{-1})	IR wavenumber (cm^{-1})	Assignment
335	–	ν (VO_4)
	374	
416		ν (Li—O)
	435	ν (Li—O)
480		ν (Li—O—Ni)
656	651	ν (Li—O—Ni)
790		ν (VO_4)
	815	[Antisymmetric stretching]
821		
	852	ν (VO_4)
	905	[Symmetric stretching]
908		

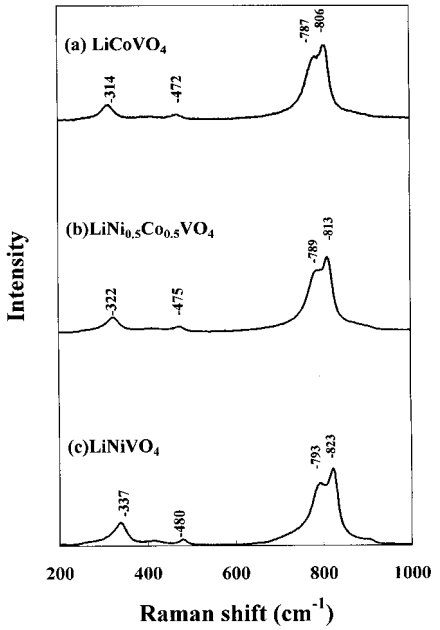

Fig. 12. Raman spectra of inverse spinel (a)$LiCoVO_4$, (b)$LiNi_{0.5}Co_{0.5}VO_4$, and (c) $LiNiVO_4$ recorded at room temperature.

from $y = 0$–0.8, reaching a minimum at $y = 0.8$. With a further increase in the Ni content (i.e. $y > 0.8$), their δ_{CSA} and η_{CSA} values actually increased. Based upon the analysis in [49], we believe that the larger δ_{CSA} value observed in samples having a high Co content is related to the larger number of Li deficiencies. Changes in the Ni/Co ratio appear to initiate structural changes reflected by changes in the δ_{CSA}. Interestingly, we noted a narrower line width in the medium Ni/Co regime for both the HT- and LT-samples in Figs. 13 and 14, and also observed a reduction in the spread of MAS side-band changing from the HT- to the LT-samples. At $y = 0.8$, the line width is the narrowest and the efg is the smallest. This may be due to a more homogeneous distribution of Ni or Co cations in the medium composition range, where the crystalline and cation defects are both at a minimum. Accordingly, the changes in MAS profile suggest that the mixed Ni/Co samples ($1 > y > 0$) contain fewer crystalline defects than the parent samples ($y = 1$ or 0), while the smaller δ_{CSA} values in the mixed Ni/Co samples should be related to the Ni and Co atom distribution.

Solid-state ^{7}Li NMR studies of inverse spinel structures in $LiNi_yCo_{1-y}VO_4$ compounds have revealed how the Li environment changed with the Ni/Co content, demonstrating that the HT-samples yielded broader Ni/Co distributions with greater crystalline defects, while the LT-samples gave much more homogeneous Ni/Co distributions with fewer defects. Prior XRD studies of these same compounds showed that the XRD patterns of all the $LiNi_yCo_{1-y}VO_4$ samples prepared by either the HT- or the LT- method were very similar to those of their inverse-spinel parent compounds, $LiNiVO_4$ and $LiCoVO_4$. While the XRD results indicated that Ni and Co are homogeneously distributed, the ^{7}Li NMR data showed that there are significant differences in the microstructure between the HT- and LT-samples. This is due to the fact that Li spin interactions are extremely sensitive to local

Table 5
Structure parameters derived from EXAFS analyses (Core V) [51]

$LiNiVO_4$	V—O			V—Ni		
Preparation method	R (Å)	N	σ^2	R (Å)	N	σ^2
Sol-gel (pH = 7)	1.93	13	0.083	3.41	12	0.014
Sol-gel (pH = 3)	1.94	14	0.011	3.41	9	0.013
Solution–coprecipitation	1.97	15	0.010	3.41	15	0.016

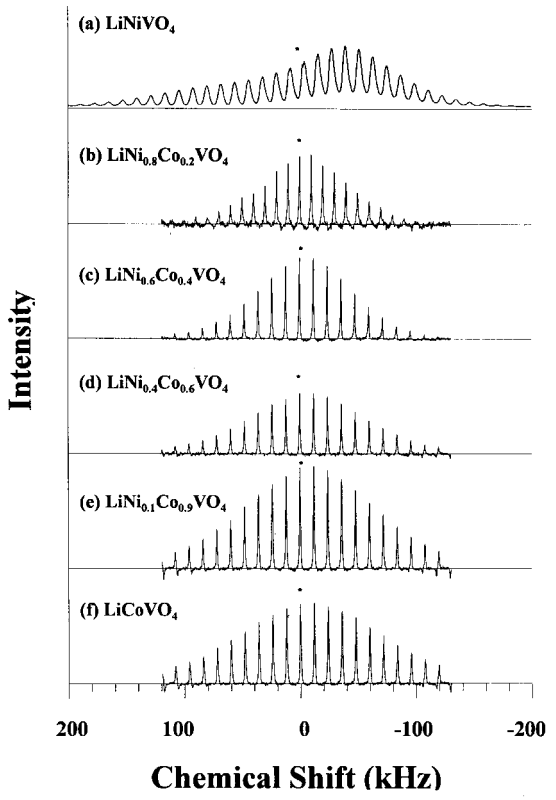

Fig. 13. Superposition of the MAS side-band manifolds for $LiNi_yCo_{1-y}VO_4$ samples prepared by the HT-method at various stoichiometries (y) [49].

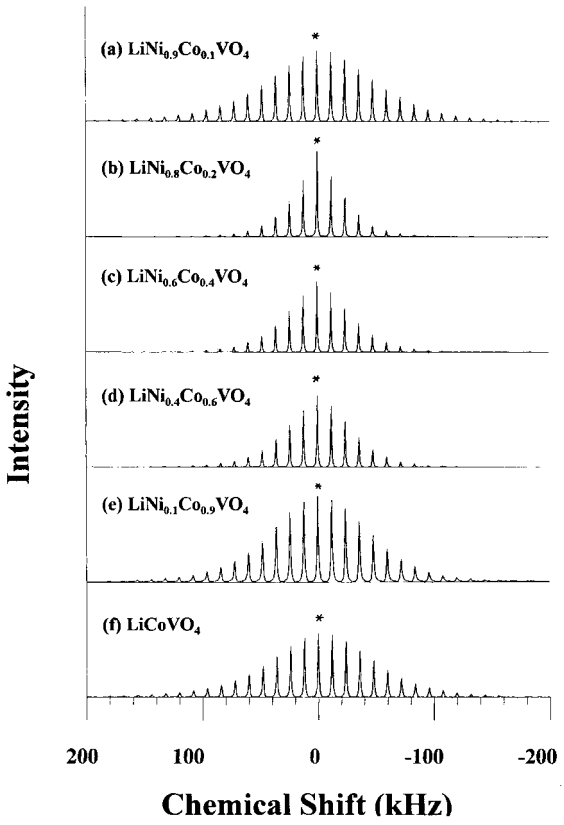

Fig. 14. Superposition of the MAS side-band manifolds for $LiNi_yCo_{1-y}VO_4$ samples prepared by the LT-method at various stoichiometries (y) [49].

crystalline defects, while the XRD technique gives bulk-averaged results, which fail to provide any information about local structural variations. More refined details of this ^7Li NMR analysis will appear in a forthcoming paper [49].

3.4. Extended X-ray absorption fine-structure spectroscopy

The local structure of the inverse spinel-type

Table 6
Structure parameters derived from EXAFS analyses (Core Ni) [50]

$LiNiVO_4$	Ni—O			Ni—V		
Preparation method	R (Å)	N	σ^2	R (Å)	N	σ^2
Sol-gel (pH = 7)	2.04	5	0.006	3.33	9	0.010
Sol-gel (pH = 3)	2.04	4	0.005	3.25	8	0.001
Solution–coprecipitation	2.03	5	0.005	3.33	9	0.010

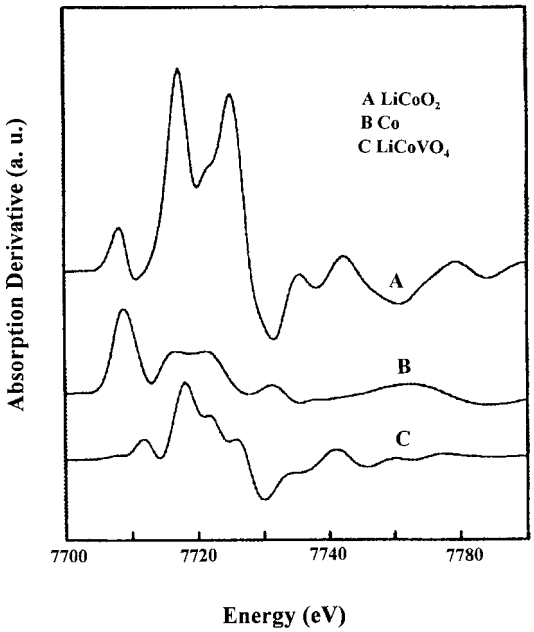

Fig. 15. The first derivative of Co-edge X-ray absorption spectra [51].

$LiNiVO_4$ samples, prepared by sol-gel and solution coprecipitation methods, was investigated by using V and Ni K-edge X-ray absorption fine structure (EXAFS) spectra [50]. Tables 5 and 6 show the structural parameters derived from the EXAFS analyses of samples prepared with different methods. It was found that the

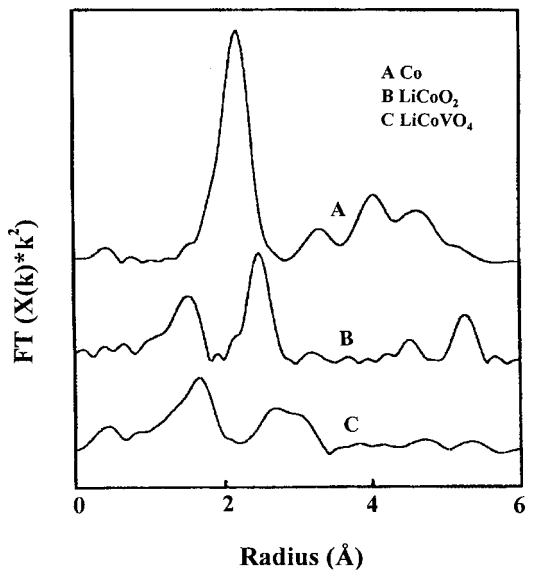

Fig. 16. Fourier transform of Co-edge X-ray absorption spectra [51].

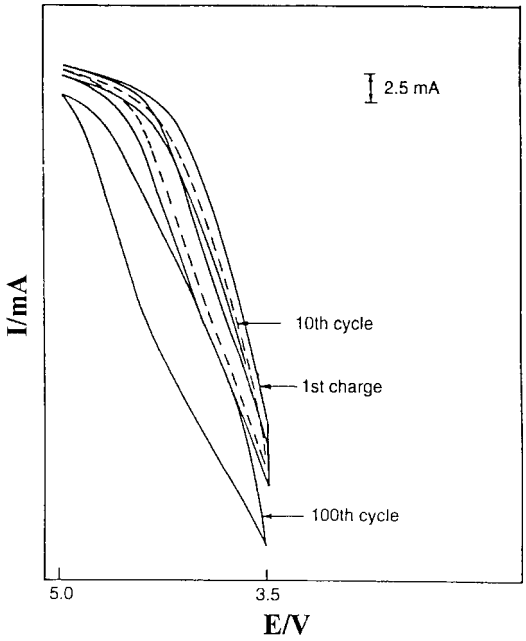

Fig. 17. Cyclic voltammogram of a $Li/LiNiVO_4$ cell employing 1 M $LiPF_6$ in an EC–DMC–MF electrolyte mixture [22].

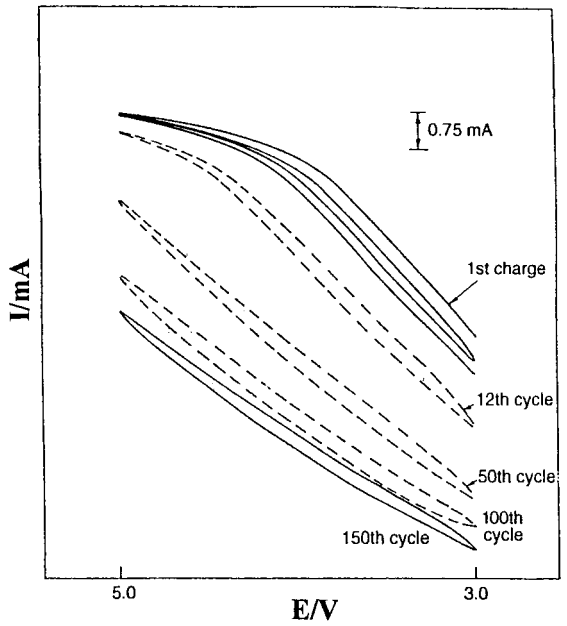

Fig. 18. Cyclic voltammogram of a $C/LiNiVO_4$ cell employing 1 M $LiPF_6$ in an EC–DMC–MF electrolyte mixture [22].

V—O, V—Ni, and Ni—O distances are 1.95 ± 0.02, 3.33 ± 0.08, and 2.03 ± 0.01 Å, respectively. The coordination number in samples prepared by the sol-gel method is smaller than that of samples prepared by a solution co-precipitation method, as shown in Tables 5 and 6, implying that the particle size of the samples prepared by a sol-gel method is smaller. This result is consistent with our prior SEM and AFM results for $LiNiVO_4$ particle size [29], using the same preparation methods.

The electronic structure of the inverse spinel-type $LiCoVO_4$ samples prepared by a solution–coprecipitation method was also investigated using K-edge X-ray absorption near edge structure (XANES) and extended X-ray absorption fine structure (EXAFS) spectra [51]. Fig. 15 displays the first derivatives of the Co-edge X-ray absorption spectra for $LiCoVO_4$, together with the $LiCoO_2$ and Co standards. Based on these results, the Co in $LiCoVO_4$ was determined to be in a low valence state, which suggests that the chemical substitution of Li^+ ions into the cathode material's structure may have contributed to that state. Fig. 16 is the Fourier transform of the X-ray absorption spectra for $LiCoVO_4$ together with those of $LiCoO_2$ and Co. The radii of the first shell Co—O and second shell Co—Co distances in the obtained cathode materials were estimated to be 1.66 and 2.81 Å, respectively, indicating that the first shell Co—O distance in $LiCoVO_4$ is larger than that in $LiCoO_2$. Meanwhile, the second shell Co—Co in $LiCoVO_4$ is also larger than that in Co and $LiCoO_2$.

4. Electrochemical properties and cell performance

4.1. Cyclic voltammetry behavior

Prabaharan et al. synthesized $LiNiVO_4$ at temperatures as low as 320°C using the aqueous glycine-nitrate combustion process and also reported on the cyclic voltammetric behavior of this compound [22]. The 2450 coin-type $Li/LiNiVO_4$ and $C/LiNiVO_4$ cells were used, with a newly developed electrolyte composition, 1 M $LiPF_6$ in an EC–DMC–MF electrolyte mixture (T = 28°C, scan rate = 10 mV/s). Graphite was used as an anode for the $C/LiNiVO_4$ cell.

The cyclic voltammograms for the $Li/LiNiVO_4$ and $C/LiNiVO_4$ cells are shown in Figs. 17 and 18, respectively, revealing the reversible nature of the material and capacity fading in the system. Both cyclic voltammograms show excellent cyclability of the material between 3 and 5 V. The $Li/LiNiVO_4$ cell in Fig. 17 displays little capacity fading, that occurred over 100 cycles, but the $C/LiNiVO_4$ cell in Fig. 18 exhibits significant capacity decay. This has been attributed to the irreversible capacity of the graphite anode [22]. There were no charge/discharge data available at this time for comparison.

Table 7
Cell performance data for $LiNiVO_4$, $LiCoVO_4$, and $LiNi_yCo_{1-y}VO_4$ cathode materials

No.	Cathode material	V-limits (V) (V vs Li)	C/D rate	1st Charge capacity ($mAhg^{-1}$)	1st Discharge capacity ($mAhg^{-1}$)	Preparation scheme number	Electrolyte	Electrode composition	Ref.
1	$LiNiVO_4$	3.0–4.9 V	0.02C	80	45	8[b]	1 M $LiPF_6$ PC–EC–DMC (1:1:2)	2% PVDF 10% CB	[8]
2	$LiNiVO_4$	3.0–4.9 V	0.1C	36	21	9[b]	1 M $LiPF_6$ EC–DEC (1:1)	5% PVDF 10% CB	[36]
3	$LiNiVO_4$	3.0–4.9 V	0.1C	77	12	14[a] pH = 3	1 M $LiPF_6$ EC–DEC (1:1)	5% PVDF 10% CB	[29]
4	$LiNiVO_4$	3.0–4.9 V	0.2C	39	24	14[a] pH = 3	1 M $LiPF_6$ EC–DEC (1:1)	5% PVDF 10% CB	[29]
5	$Li_{0.89}Ni_{1.11}VO_4$	3.0–4.9 V	0.02C	50	16	11[b]	1 M $LiBF_4$ EC–PC–DMC (1:1:3.9)	2% PVDF 10% CB	[37]
6	$Li_{0.96}Ni_{1.04}VO_4$	3.0–4.9 V	0.02C	46	19	11[b]	1 M $LiBF_4$ EC–PC–DMC (1:1:3.9)	2% PVDF 10% CB	[37]
7	$Li_{1.03}Ni_{0.97}VO_4$	3.0–4.9 V	0.02C	32	15	11[b]	1 M $LiBF_4$ EC–PC–DMC (1:1:3.9)	2% PVDF 10% CB	[37]
8	$LiNiVO_4$	3.0–4.9 V	0.1C	43	29	14[a] pH = 1	1 M $LiPF_6$ EC–DEC (1:1)	5% PVDF 10% CB	[54]
9	$LiNiVO_4$	3.0–4.9 V	0.1C	43	24	14[a] pH = 2	1 M $LiPF_6$ EC–DEC (1:1)	5% PVDF 10% CB	[54]
10	$LiNiVO_4$	3.0–4.9 V	0.1C	40	24	14[a] pH = 3	1 M $LiPF_6$ EC–DEC (1:1)	5% PVDF 10% CB	[54]
11	$LiNiVO_4$	3.0–4.9 V	0.1C	37	21	14[a] pH = 4	1 M $LiPF_6$ EC–DEC (1:1)	5% PVDF 10% CB	[54]
12	$LiNiVO_4$	3.0–4.9 V	0.1C	29	19	14[a] pH = 5	1 M $LiPF_6$ EC–DEC (1:1)	5% PVDF 10% CB	[54]
13	$LiNiVO_4$	3.0–4.9 V	0.1C	21	15	14[a] pH = 6	1 M $LiPF_6$ EC–DEC (1:1)	5% PVDF 10% CB	[54]
14	$LiCoVO_4$	3.0–4.5 V	0.1C	65	33	19[a]	1 M $LiClO_4$ EC–PC–DMC (1:1:2)	10% EPDM 10% CB	[35]
15	$LiCoVO_4$	3.0–4.5 V	0.1C	101	71	17[b]	1 M $LiClO_4$ EC–PC (1:1)	10% EPDM 10% CB	[36]
16	$LiCoVO_4$	3.0–4.5 V	0.1C	99	64	19[a]	1 M $LiClO_4$ EC–PC (1:1)	10% EPDM 10% CB	[36]
17	$LiCoVO_4$	3.0–4.5 V	0.1C	62	37	17[b]	1 M $LiClO_4$ EC–PC (1:1)	10% EPDM 10% CB	[36]
18	$LiCoVO_4$	3.0–4.5 V	0.1C	50	29	17[b]	1 M $LiPF_6$ EC–PC–DMC (1:1:2)	10% EPDM 10% CB	[36]
19	$LiCoVO_4$	3.0–4.5 V	0.1C	63	40	17[b]	1 M $LiBF_4$ EC–PC–DMC (1:1:4)	10% EPDM 10% CB	[8]
20	$LiCoVO_4$	3.0–4.5 V	0.1C	69	47	19[a]	1 M $LiBF_4$ EC–PC–DMC (1:1:4)	10% EPDM 10% CB	[36]
21	$LiNi_{0.5}Co_{0.5}VO_4$	3.0–4.5 V	0.1C	52	36	A[c]	1 M $LiClO_4$ EC–PC (1:1)	10% EPDM 10% CB	[36]
22	$LiNi_{0.5}Co_{0.5}VO_4$	3.0–4.5 V	0.1C	40	21	A[c]	1 M $LiPF_6$ EC–PC–DMC (1:1:2)	10% EPDM 10% CB	[36]
23	$LiNi_{0.5}Co_{0.5}VO_4$	3.0–4.5 V	0.1C	50	35	A[c]	1 M $LiBF_4$ EC–PC–DMC (1:1:4)	10% EPDM 10% CB	[36]
24	$LiNi_{0.5}Co_{0.5}VO_4$	3.0–4.5 V	0.1C	67	44	B[d]	1 M $LiBF_4$ EC–PC–DMC (1:1:4)	10% EPDM 10% CB	[36]
25	$LiNi_{0.2}Co_{0.8}VO_4$	3.0–4.5 V	0.1C	59	31	C[e]	1 M $LiClO_4$ EC–PC–DMC (1:1:2)	10% EPDM 10% CB	[35]
26	$LiNi_{0.1}Co_{0.9}VO_4$	3.0–4.5 V	0.1C	80	44	C[e]	1 M $LiClO_4$ EC–PC–DMC (1:1:2)	10% EPDM 10% CB	[35]

[a] Low-temperature solution–coprecipitation process.
[b] High-temperature solid-state process.
[c] $Li_2CO_3 + NiO + Co_3O_4 + V_2O_5$, 730°C, 12 h.
[d] $LiOH + Ni(NO)_3{\cdot}6H_2O + Co(NO)_3{\cdot}6H_2O + NH_4VO_3$, 500°C, 48 h.
[e] $LiOH + Ni(NO)_3{\cdot}6H_2O + Co(NO)_3{\cdot}6H_2O + NH_4VO_3$, 800°C, 12 h.

4.2. Electrical conductivity

Although interest in the new high voltage inverse spinel materials has increased, little has been reported on their electrical conductivity. Using the dc four-terminal method [34], Ito et al. investigated the electrical conductivity of $LiNiVO_4$ and $LiCoVO_4$ between 450 and 1050°C [52] and subsequently between 450 and 1000°C in air. According to their data, the ionic conductivity was insignificant and the electrical conductivity of $LiNiVO_4$ at 450°C was in the order of 10^{-5} S/cm [34]. However, our preliminary measurements were in the order of 10^{-8} S/cm at ambient temperature.

$LiNiVO_4$ is a poor electrical conductor. Therefore, it must be mixed with significant amounts of binder and a good electrical conductor such as carbon black to ensure that the electrode will deliver sufficient electrical conductivity, but carbon black lowers the electrode material's energy density.

Another common way to increase electrical conductivity is to use a dopant or an additive. Liang found that the conductivity of lithium iodide could be increased substantially, from 10^{-7} to 10^{-5} S/cm at 25°C, through the incorporation of aluminum oxide [53]. In fact, after the incorporation of trace amounts of the lanthanum element, the electrical conductivity of $LiNiVO_4$ increased significantly, but no conductivity improvement was observed for $LiCoVO_4$ [24]. Measurements were taken at 25°C using the dc polarization method. The conductivity of the smallest Yb-doped samples improved the most, from 10^{-10} to 10^{-7} S/cm, at a mole ratio of $LiNiVO_4$–Yb = 10^4:1, while still maintaining a high conductivity of 10^{-7} S/cm, up to a mole ratio of 10^2. The conductivity of medium Gd-doped samples peaked at around 6.21×10^{-7}–3.52×10^{-7} S/cm at a mole ratio of 10^4, but above that rapidly declined to 10^{-10} S/cm. The conductivity of the largest La-doped samples only showed a slight increase, from 10^{-9} to 10^{-8} S/cm, at a mole ratio of 10^4. During the doping process at lower dopant concentrations, the activation energy decreased as the concentration increased, but it remained virtually constant at higher dopant concentrations, due to reactions between $LiNiVO_4$ and the dopants [24].

4.3. Cathode performance

The electrochemical properties and cell performance for $LiNiVO_4$, $LiCoVO_4$ and $LiNi_yCo_{1-y}VO_4$ are listed in Table 7. The table contains information regarding the cathode materials, cycling conditions, initial capacities, preparation scheme numbers, electrolytes, and electrode compositions. Li metal foil was used as a counter electrode in 2325 coin-type cells. Each cell test entry is numbered in the first column, while literature references are given in the last column in Table 7. The preparation scheme numbers for the first 20 entries correspond to those in Table 1, which lists the preparation methods and reaction conditions for $LiNiVO_4$ and $LiCoVO_4$. Entries 21–26 used the preparation schemes A–C described at the end of Table 7.

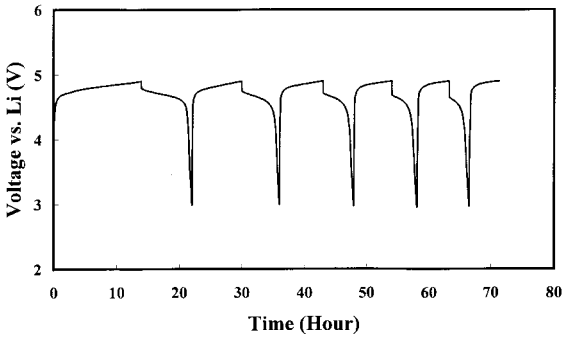

Fig. 19. Voltage vs time curve for a Li/$LiNiVO_4$ cell.

4.3.1. $LiNiVO_4$ electrode performance

So far, only a few researchers have reported on the charge/discharge performance of cells using $LiNiVO_4$, $LiCoVO_4$, or $LiNi_yCo_{1-y}VO_4$ as electrode materials in lithium secondary batteries. Fig. 19 shows a diagram of the voltage vs time for a Li/ $LiNiVO_4$ coin cell (#1), which displayed a very high voltage of 4.8 V. Based on in-situ X-ray cell results [8], the inverse spinel structure of $LiNiVO_4$ is not destroyed during charging to 5.3 V, and lithium atoms in $LiNiVO_4$ can be reversibly extracted and reinserted near 4.8 V vs Li metal. The removal of lithium, corresponding to $x = 1$ in Li_xNiVO_4, is equivalent to a theoretical capacity of 148 mAh/g. A capacity of up to about 80 mAh/g was attained during the first charge to 4.9 V, but only about a capacity of 45 mAh/g was attained during the next discharge.

Similarly, the Li/$LiCoVO_4$ cell (#19) demonstrated a better cycle life, as shown in Fig. 20, but the reversible capacity was only 40 mAh/g. Fig. 20 displays the cycle behavior of a Li/$LiCoVO_4$ cell, consisting of two curves: (a) a voltage vs time curve and (b) a differential chronopotentiometric curve. The derivative plot in Fig. 20(b) shows that two peaks at 4.07 and 4.13 V were observed during the charging and discharging process, respectively. The actual cell capacity was much smaller than the theoretical capacity that had been expected from the complete removal of Li from $LiNiVO_4$ or $LiCoVO_4$. We believe that the discharge capacity being on the low end of the achievable capacity was caused by the material's structure or by electrolyte oxidation problems that occurred under these conditions. Clarifying and overcoming these problems is an important future task for us.

The high voltage features of the inverse spinel cath-

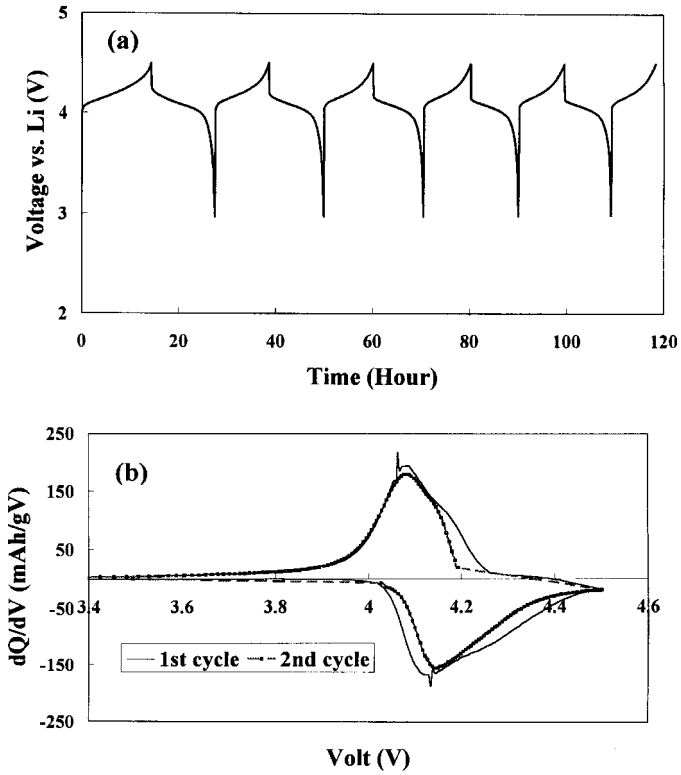

Fig. 20. Voltage vs time curve for a Li/$LiCoVO_4$ cell: (a) voltage vs time curve; (b) differential chronopotentiometric curve.

odes, as well as a comparison with some other important lithiated transition metal oxides and sulfides, and their approximate working voltages with respect to the lithium metal electrodes are shown in Fig. 21. For simplicity, $LiNi_yCo_{1-y}VO_4$ materials are not included. The voltage range of the individual cathode materials shown depends upon the lithiation depth, x, or the number of reacting lithium atoms. Δx denotes the lithiation range, in which reversible capacity can be attained. The voltage range of both $LiNiVO_4$ and $LiCoVO_4$ is small and the exact x range for both vanadates has not yet been determined.

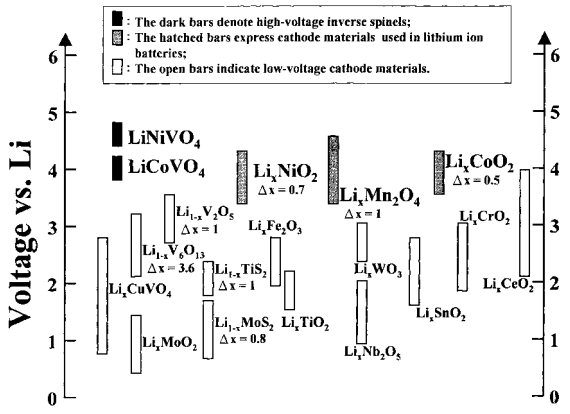

Fig. 21. Approximate working voltage of lithiated transition metal oxides and sulfides. The horizontal position has no significance and the values of reversible range (Δx) were obtained from [55].

4.3.1.1. Synthesis temperature effect on cell capacity. In the previous high-voltage inverse spinel work [8], we used a high-quality electrolyte with proprietary additives provided by a private company. In our more recent work, we were limited to using the best commercially available electrolyte and cell performance was not so high. However, we are aware of the reality that our goal at this stage is not to achieve the highest cell performance, but rather to investigate the effect on various factors on the performance of the cell.

At higher preparation temperatures, the cell capacity diminished significantly. For example, cells incorporating cathode materials prepared at 600°C had a higher charge capacity of 48 mAh/g, compared to those with cathode materials prepared at 975°C, which only had a charge capacity of 32 mAh/g [37]. We make a conjecture that lithium reacted with the preparation vessel substrate, resulting in lithium mass loss and partially

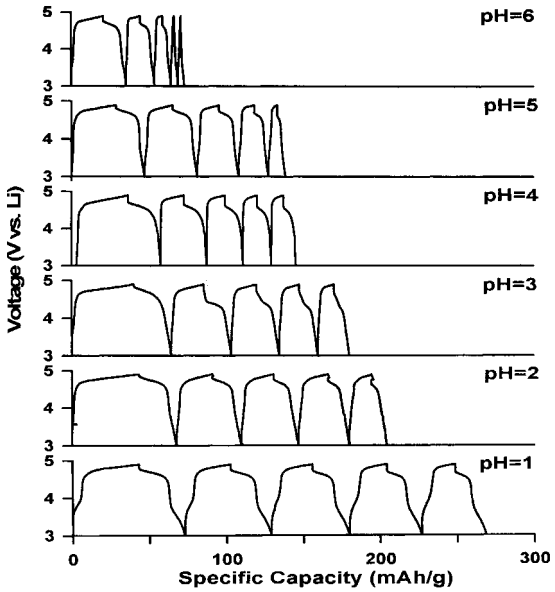

Fig. 22. Voltage vs time curves for Li/$LiNiVO_4$ cells with cathode materials prepared at various pH values [54].

fused tunnels, where mobile lithium ions could not move freely.

4.3.1.2. pH effect on cell capacity. $LiNiVO_4$ cathode materials were prepared by a sol-gel method at various pH values, ranging from 1 to 6 [54]. Coin cells (#8–13) using these cathode materials were charged to 4.9 V at a 0.1*C* rate. Their voltage vs time curves are plotted in Fig. 22. The cathode material prepared at pH = 1 showed the best cell performance, with an initial charge capacity of 43 mAh/g and a discharge capacity of 29 mAh/g. Furthermore, the $LiNiVO_4$ sample prepared at pH = 1 decayed much more slowly than those samples having other pH values. Detailed data indicating capacity versus cycle with various pH values are listed in Table 8.

Table 8
Capacity data of Li/$LiNiVO_4$ cells with cathode materials prepared at various pH values [54][a]

Cycle no.	Cycle 1		Cycle 2		Cycle 3		Cycle 4		Cycle 5	
	CC	DC	CC	DC	CC	DC	CC	DC	CC	DC
pH = 1	43	29	30	26	27	24	25	22	22	20
CE		67%		87%		89%		88%		91%
pH = 2	43	24	23	19	21	16	19	14	14	10
CE		56%		83%		76%		74%		71%
pH = 3	40	24	21	18	16	15	13	12	11	10
CE		60%		86%		94%		92%		91%
pH = 4	38	21	15	15	12	12	9	9	8	8
CE		57%		100%		100%		100%		100%
pH = 5	29	19	18	16	14	13	10	9	6	5
CE		66%		89%		93%		90%		83%
pH = 6	21	15	9	9	5	5	2	2	2	2
CE		71%		100%		100%		100%		100%

[a] CC, charge capacity (mAh/g); DC, discharge capacity (mAh/g); CE, cycle efficiency (%).

4.3.2. $LiCoVO_4$ electrode performance

Although $LiNiVO_4$ has a very high cell voltage, 4.8 V, it has been difficult to apply as a cathode, because most electrolytes are not electrochemically compatible. However, the $LiCoVO_4$ system exhibits a lower voltage of 4.2 V, which makes it more suitable for some oxidation-resistant electrolytes below 4.8 V. Many attempts (#14–20 in Table 7) have been made to improve the capacity performance of Li/$LiCoVO_4$ cells by using different preparation methods or electrolyte compositions. Of these, cases #15 and #16 show the best cell capacity results. Further measurements, using different electrolytes compositions, cathode fabrication methods, and formation conditions are in progress.

4.3.3. $LiNi_yCo_{1-y}VO_4$ ($0 \leq y \leq 1$) electrode performance

There is a significant voltage difference between $LiNiVO_4$ (4.8 V) and $LiCoVO_4$ (4.2 V), implying that the voltage behavior is affected by the presence and location of nickel atoms. A solid solution combining $LiNiVO_4$ and $LiCoVO_4$ could theoretically optimize cell voltage and performance and help us to better understand the effects of nickel atoms on the crystal structure and Li intercalation/deintercalation of $LiMVO_4$ inverse spinels.

A series of $LiNi_yCo_{1-y}VO_4$ compounds ($0 \leq y \leq 1$) were synthesized and characterized for cell evaluation. A large number of samples and tests were involved; only a few typical cell tests (#21–26) have been included in Table 7. In order to obtain representative results, $LiNi_{0.5}Co_{0.5}VO_4$ was selected, since it was in the middle of the series. Table 9 presents a comparison of selected capacity data for Li/ $LiNi_yCo_{1-y}VO_4$ cells (where $y = 0$ or $y = 0.5$), with the cathode materials prepared by either the HT- or the LT-method [21]. The electrolyte used in the tests was 1 M $LiBF_4$ in an EC–PC–DMC (volume ratio = 1:1:4) mixture. In general, the charge/discharge capacity of a Li/ $LiNi_{0.5}Co_{0.5}VO_4$ cell is compatible with that of a Li/ $LiCoVO_4$ cell. In terms of electrode preparation, the LT-method offers a small advantage in terms of capacity over the HT-method. All cells suffered a large irreversible loss in overall capacity in the first cycle, but stabilized in terms of cycle efficiency during later cycling.

Table 9
Capacity data of $Li/LiNi_yCo_{1-y}VO_4$ cells (where $y = 0$ or 0.5) with cathode materials prepared by either the HT- or LT-method [21]

Cycle	$y = 0.0$			$y = 0.5$		
	Charge capacity (mAh/g)	Discharge capacity (mAh/g)	Cycle efficiency (%)	Charge capacity (mAh/g)	Discharge capacity (mAh/g)	Cycle efficiency (%)
HT method						
1st	63	40	64	50	35	69
2nd	44	38	86	40	34	85
3rd	33	29	88	37	33	90
4th	38	35	90	34	31	91
5th	33	29	88	40	37	91
LT method						
1st	69	47	67	67	44	65
2nd	36	32	88	34	30	89
3rd	31	28	90	29	26	92
4th	30	26	88	27	25	91
5th	28	24	89	27	25	92

4.4. Anode performance

Tarascon and his co-workers [23] used amorphous $LiNiVO_4 \cdot 2.6H_2O$ dried at 50°C as the positive electrode and Li as the negative electrode. The voltage–composition curve of a $LiNiVO_4.2.6H_2O/Li$ cell is shown in Fig. 23. On the first discharge, $LiNiVO_4$ reacted with 10.5 mole lithium ions per formula unit, while only 7.5 could be removed upon the following charge. This irreversible capacity loss was possibly due to the presence of residual water within the amorphous phase. However, the crystallized $LiNiVO_4$ could reversibly react with 7 lithiums per formula unit, which is equivalent to a capacity of 920 mAh/g, almost 2.5 times the capacity of a conventional graphite electrode.

For comparison, Table 10 presents the cell performance data for two $LiNiVO_4$ samples: one prepared by the LT-method and the other by the HT-method. The LT-sample enjoyed a slight advantage in discharge capacity (1110 vs 1025 mAh/g), but suffered a large loss in irreversible capacity (444 vs 260 mAh/g) compared to the HT-sample. It appears that the irreversible capacity loss is associated with the BET surface area of $LiNiVO_4$ and the amount of adsorbed water within the material. Note that the amount of adsorbed water can be reduced and is related to irreversible capacity loss. Furthermore, these $LiNiVO_4$ materials prepared by either the LT- or HT-method all displayed poor capacity retention upon cycling over the 0.02–3 V range.

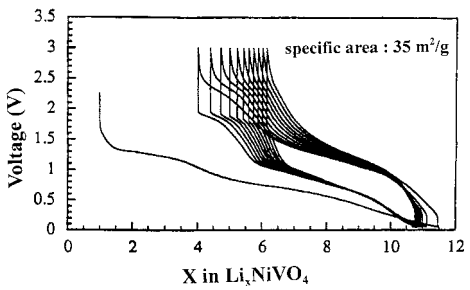

Fig. 23. Voltage vs composition curve for an amorphous $LiNiVO_4 \cdot 2.6H_2O/Li$ cell [23].

Tarascon's investigation [23] confirmed that vanadates can be used as negative electrodes in lithium batteries, because they can accommodate large amounts of lithium at an average voltage of less than 1 V. However, further work is necessary because regardless of the conditions used, large capacity fading was observed, although it has not yet been determined whether the fading is an intrinsic or extrinsic characteristic of the vanadate electroactive material. A decrease in the cell capacity appears to be accompanied by a larger polarization. At first glance, this could mean that polarization and capacity fading are related. One possible reason for the increase in polarization could be the formation of a passivating film due to the decomposition of the electrolyte or the electroactive material into a poorly conducting phase. Further studies on the cycle-life of $LiNiVO_4/Li$ cells using various electrolytes should help clarify the above.

5. Conclusions

$LiNiVO_4$, $LiCoVO_4$ and related $LiNi_yCo_{1-y}VO_4$ ($0 < y < 1$) compounds are possible 4-V or higher cathode candidates for lithium ion batteries. However, any practical application depends upon resolving the

Table 10
Cell performance data for $LiNiVO_4$ anode materials

Anode material	V-limits (V) (V vs Li)	C/D rate	1st Charge capacity ($mAhg^{-1}$)	1st Discharge capacity ($mAhg^{-1}$)	Preparation condition	Electrolyte	Electrode composition	Ref.
LT-$LiNiVO_4$	0.02–3.0 V	1 Li/2 h	1554	1110	$LiNO_3 + Ni(NO)_3{\cdot}6H_2O + NH_4VO_3$ 200–700°C 12 h in air	1 M $LiPF_6$ EC–DMC (2:1)	15% PVDF-HFP 6% SP 23% DBP	[23]
HT-$LiNiVO_4$	0.02–3.0 V	1 Li/2 h	1285	1025	$LiOH{\cdot}H_2O + NiO + V_2O_5$ 750°C 12 h in O_2	1 M $LiPF_6$ EC–DEC (1:1)	5% PVDF 10% KS6	[54]

electrolyte decomposition problem. $LiNiVO_4$ is also a very promising anode material with a high cell capacity. In this case, the problem is poor capacity retention and a large loss in initial capacity.

In the area of electrode material research, many studies have been done on spinel materials such as $LiMn_2O_4$, which has already been successfully used as a cathode material in the $C/Li_{1+x}Mn_2O_4$ lithium ion batteries. In contrast, there have been fewer extensive studies on inverse spinel materials, but our results show that further research would be promising, due to their potential cathode and anode applications.

Before the development of a commercially viable cell can become a reality, much work must be done in the following areas: (1) developing electrolytes with an oxidation resistance of at least 5 V; (2) understanding Li ion diffusion and mobility in an inverse spinel structure; (3) solving the polarization and capacity fading problems; (4) achieving a fundamental understanding of the large Li-acceptance in these materials; (5) determining how Li deficiency, particle size, surface area, and adsorbed water content relate to the preparation methods.

Over the last few years, different synthesis methods have been developed for producing interesting pure cathode materials. Several synthesis routes have utilized to improve cell performance, including the conventional ceramic sintering, solution co-precipitation, sol-gel, and hydrothermal methods. So far, new preparation methods have made no great improvements in the cell performance of $LiNiVO_4$ or related materials. The major problems to be overcome have been mentioned above. Since research on inverse spinel electrode materials is in its infancy, many scientific and technical challenges still remain in developing these promising materials.

Acknowledgements

Financial support from the National Science Council of the Republic of China is gratefully acknowledged. The authors would like to thank Professor J. M. Nester of the Department of Physics, National Central University, for useful discussions and suggestions.

References

[1] J.C. Bernier, P. Poix, A. Michel, Compt. Rend. Acad. Sci. (Paris) 253 (1961) 1578.
[2] J.C. Bernier, P. Poix, A. Michel, Bull. Soc. Chim. France, 1661 (1963).
[3] G. Blasse, J. Inorg. Nucl. Chem. 25 (1963) 136.
[4] G. Blasse, Philips Res. Rept. Suppl. No. 3, 1964.
[5] A. Durif, J.C. Joubert, J.C. Grenier, Compt. Rend. Acad. Sci. (Paris) 260 (1965) 2472.
[6] M.Th Paques-Ledent, P. Tarte, Spectrochimica Acta 30A (1974) 673.
[7] R. Kanno, Y. Kawamoto, Y. Takeda, M. Hasegawa, O. Yamamoto, Solid State Ionics 40/41 (1980) 576.
[8] G.T.K. Fey, W. Li, J.R. Dahn, J. Electrochem. Soc. 141 (1994) 2279.
[9] M.M. Thackeray, W.I.F. David, J.B. Goodenough, Mat. Res. Bull. 17 (1982) 785.
[10] L.A. de Picciotto, M.M. Thackeray, Mat. Res. Bull. 21 (1986) 583.
[11] G.T.K. Fey, J.R. Dahn, US Patent 5,518,842, 1996.
[12] M. Armand, in: D.W. Murphy, J. Broadhead, B.C.H. Steele (Eds.), Materials for Advanced Batteries, Plenum Press, New York, 1980, p. 145.
[13] S. Basu, US Patent, 4,423,125, 1983.
[14] M. Lazzari, B. Scrosati, J. Electrochem. Soc. 127 (1980) 773.
[15] J.O. Besenhard, P. Komenda, A. Paxinos, E. Wudy, M. Josowicz, Solid State Ionics 18/19 (1986) 823.
[16] J. Wang, I.D. Raistrick, R.A. Huggins, J. Electrochem. Soc. 133 (1986) 457.
[17] K. Mizushima, P.C. Jones, P.J. Wiseman, J.B. Goodenough, Mater. Res. Bull. 15 (1980) 783.
[18] J.R. Dahn, U. von Sacken, M.W. Juzkow, H. Al-Janaby, J. Electrochem. Soc. 138 (1991) 2207.
[19] J.M. Tarascon, D. Guyomard, Electrochim. Acta 38 (1993) 1221.
[20] T. Ohzuku, A. Ueda, M. Nagayama, J. Electrochem. Soc. 140 (1993) 1862.
[21] G.T.K. Fey, K.S. Wang, S.M. Yang, J. Power Sources 68 (1997) 159.
[22] S.R.S. Prabaharan, M.S. Michael, S. Radhakrishna, C. Julien, J. Mater. Chem. 7 (1997) 1791.
[23] F. Orsini, E. Baudrin, S. Denis, L. Dupont, M. Touboul, D. Guyomard, Y. Piffard, J.M. Tarascon, J. Solid State Ionics 107 (1998) 123.
[24] G.T.K. Fey, C.S. Wu, Pure & Appl. Chem. 69 (1997) 2329.
[25] A.K. Padhi, W.B. Archibald, K.S. Nanjundaswamy, J.B. Goodenough, J. Solid State Chemistry 128 (1997) 267.
[26] G.T.K. Fey, W.B. Perng, Materials Chemistry and Physics 47 (1997) 279.
[27] A. Durif, J.C. Joubert, J.C. Grenier, Compt. Rend. Acad. Sci. (Paris) 260 (1965) 2472.
[28] L.L.Y. Chang, F.Y. Wang, J. Amer. Cera. Soc. 71 (1988) 689.
[29] G.T.K. Fey, K.S. Chen, J. Power Sources, 1999 (in press).
[30] C.H. Lu, W.C. Lee, S.J. Liou, G.T.K. Fey, J. Power Sources, 1999 (in press).
[31] M.M. Aslanukova, A.M. Khubiev, E.G. Semin, J. Appl. Chem., USSR 53 (1980) 1880.
[32] R. Kanno, Y. Takeda, M. Hasegawa, Y. Kawamoto, O. Yamamoto, J. Solid State Chem. 94 (1991) 319.
[33] S. Suzuki, M. Tomita, S. Okada, H. Arai, J. Phys. Chem. Solids 58 (1997) 799.
[34] Y. Ito, Nippon Kagaku Kaishi 11 (1979) 1483.

[35] K.S. Wang, Master thesis, National Central University, Taiwan, ROC, 1995.
[36] S.M. Yang, Master thesis, National Central University, Taiwan, ROC, 1995.
[37] G.T.K. Fey, J.R. Dahn, M.J. Zhang, W. Li, J. Power Sources 68 (1997) 549.
[38] M. Touboul, A. Popot, Rev. Chim. Miner. 22 (1985) 610.
[39] D.W. Murphy, R.J. Cava, S.M. Zahurak, A. Santoro, Solid State Ionics 9 (10) (1983) 413.
[40] T. Ohzuku, M. Kitagawa, T. Hirai, J. Electrochem. Soc. 137 (1990) 769.
[41] Y. Ito, T. Maruyama, T. Nakamura, Y. Saito, Report of the research Laboratory of Engineering Materials, Tokyo Institute of Technology, 11, 11, 1986.
[42] G.T.K. Fey, unpublished results.
[43] S. Hayakawa, T. Yoko, S. Sakka, Bull. Chem. Soc. Jpn 66 (1993) 3393.
[44] S. Hayakawa, T. Yoko, S. Sakka, J. Ceram. Soc. Jpn 102 (1994) 530.
[45] S. Hayakawa, T. Yoko, S. Sakka, J. Solid-State Chem. 112 (1994) 329.
[46] M. Menetrier, A. Rougier, C. Delmas, Solid State Comm. 90 (1994) 439.
[47] M. Carewska, S. Scaccia, F. Croce, S. Arumugam, Y. Wang, S. Greenbaum, Solid State Ionics 93 (1997) 227.
[48] J. Sugiyama, T. Atsumi, A. Koiwai, T. Sasaki, T. Hioki, N. Kamegashira, J. Phys. Condens. Matter. 9 (1997) 1729.
[49] P.P. Chu, D.L. Huang, G.T.K. Fey, Proceedings of '99 Asian Conference on Electrochemistry, Tokyo, Japan, May, 1999.
[50] B.J. Hwang, Y.W. Tsai, G.T.K. Fey, J.F. Lee, Proceedings of Fourth SRRC Users' Meeting, Hsin-chu, Taiwan, ROC, 17–21 November, 1998.
[51] B.J. Hwang, Y.W. Tsai, G.T.K. Fey, J.F. Lee, Proceedings of Third SRRC Users' Meeting, Hsin-chu, Taiwan, ROC, 5–7 November, 1997.
[52] Y. Ito, T. Maruyama, Y. Saito, Nippon Kagaku Kaishi 8 (1986) 1069.
[53] C.C. Liang, J. Electrochem. Soc. 120 (1973) 1289.
[54] Z.Y. Yuan, Master thesis, National Central University, Taiwan, ROC, 1999.
[55] K. Brandt, Solid State Ionics 69 (1994) 173.